RSC Advances

PAPER

Cite this: *RSC Adv.*, 2016, **6**, 74878

Advances in photocatalytic NO_x abatement through the use of Fe_2O_3/TiO_2 nanocomposites†

José Balbuena,[a] Giorgio Carraro,*[b] Manuel Cruz,[a] Alberto Gasparotto,[b] Chiara Maccato,[b] Adrián Pastor,[a] Cinzia Sada,[c] Davide Barreca[d] and Luis Sánchez*[a]

Received 20th June 2016
Accepted 1st August 2016

DOI: 10.1039/c6ra15958c

www.rsc.org/advances

Supported Fe_2O_3/TiO_2 nanocomposites were prepared for the first time by a plasma-assisted route and successfully tested in photocatalytic NO_x abatement driven by solar illumination. In particular, a sequential low-temperature (<100 °C) plasma enhanced-chemical vapor deposition (PE-CVD)/radio frequency (RF) sputtering approach was used to fabricate Fe_2O_3/TiO_2 nanocomposites with controlled composition and morphology. The preparation process was accompanied by a thorough multi-technique investigation carried out by complementary techniques, including X-ray photoelectron spectroscopy (XPS), secondary ion mass spectrometry (SIMS), field emission-scanning electron microscopy (FE-SEM), X-ray diffraction (XRD), and atomic force microscopy (AFM). The results evidenced the formation of high purity nanocomposites, in which TiO_2 content could be tailored by controlled variations of the sole sputtering time, and characterized by an intimate Fe_2O_3/TiO_2 contact, of key importance to exploit the chemical and electronic coupling between the two oxides. The obtained nanomaterials were tested in NO photo-oxidation activated by sunlight, showing a remarkable activity in NO_x ($NO + NO_2$) removal and a high selectivity (>60%) in their conversion to nitrate species. Overall, the present performances candidate the present photocatalysts as valuable materials for next-generation technologies aimed at the abatement of harmful gaseous pollutants.

1 Introduction

In modern society, atmospheric pollution has been recognized as one of the most severe threats for both the environment and human health. Among the most important primary pollutants, NO_x (NO and NO_2) trigger the production of tropospheric ozone and acid rains, and, in addition, severely affect respiratory and immune systems.[1–4] As a consequence, the control of NO_x emissions has been largely regulated by environmental legislation, which limits their allowed hourly concentration below 0.2 ppm.[1,5] In spite of these requirements, the above value is still often exceeded especially in big cities,[6,7] rendering the efficient NO_x removal (De-NO_x) a main open challenge for environmental remediation purposes.[8–11]

In this regard, photocatalysis has emerged as a viable technology, as testified by the growing number of commercial products available on the market and the increasing scientific interest on related processes.[1,3,5] In fact, the possibility of carrying out photocatalytic air remediation in the presence of sunlight, atmospheric oxygen and water – abundant and largely available natural resources – opens attractive perspectives for the development of "green" daylight-driven processes.[1,5] This possibility has paved the way to the integration of depolluting materials in advanced building components, ranging from photocatalytic pavements and mortars to windows and paints, in an attempt to achieve an effective NO_x de-pollution in urban areas.[12,13] In particular, TiO_2-based photocatalysts (PCs) have been widely exploited thanks to titania favorable properties, including chemical inertness, long-term stability and low cost.[5,14–18] Nevertheless, the relatively large band gap of TiO_2 ($E_G \approx 3.2$ eV) enables the harvesting of the sole UV light, accounting for only ≈5% of the incoming solar energy.[3,19] Therefore, the development of alternative sunlight-activated photocatalysts with high efficiency and stability is highly demanded. Among the various strategies proposed to extend radiation absorption into the visible (Vis) range, such as doping and dye photosensitization,[11,14,17,20] a proficient way concerns the fabrication of nanocomposite systems, such as Fe_2O_3/TiO_2.[21–24] Fe_2O_3, a non-toxic and largely available semiconducting oxide ($E_G = 2.2$ eV), can in fact enable to extent light absorption into the Vis range, but is characterized by a fast electron–hole recombination,

[a]*Department of Inorganic Chemistry and Engineering Chemistry, Córdoba University, 14071 Córdoba, Spain. E-mail: luis-sanchez@uco.es*

[b]*Department of Chemistry, Padova University and INSTM, 35131 Padova, Italy. E-mail: giorgio.carraro@unipd.it*

[c]*Department of Physics and Astronomy, Padova University and INSTM, 35131 Padova, Italy*

[d]*ICMATE-CNR and INSTM, Department of Chemistry, Padova University and INSTM, 35131 Padova, Italy*

† Electronic supplementary information (ESI) available: XRD, XPS, SEM, AFM, IR and photocatalytic data. See DOI: 10.1039/c6ra15958c

resulting in poor photocatalytic performances.[25–28] Attempts to circumvent these problems have included the control of Fe_2O_3 nano-organization, as well as its chemical modification by doping, surface passivation or functionalization with suitable systems.[19,23,28,29] In particular, the design of Fe_2O_3/TiO_2 nanocomposites is expected to provide an improved efficiency in solar-driven De-NO_x processes, synergistically exploiting the favorable properties of single-phase components and reducing, at the same time, their disadvantages.[21,28] Indeed, as also reported for other composite systems, TiO_2 coupling with other materials can enhance visible light absorption, and results in an effective separation of photogenerated electron–hole pairs and fast interfacial charge transfer.[30–32] Up to date, Fe_2O_3/TiO_2 nanosystems in powdered form have been obtained by means of various routes and used for many photo-assisted dye degradation processes in the liquid phase,[21,24,33–36] whereas only a few TiO_2-based composites (*i.e.* N–TiO_2/Fe_2O_3 [37] and N–TiO_2/ZrO_2 [38]) were studied for gas phase De-NO_x photocatalytic processes. In addition, only a few reports have so far been dedicated to Fe–Ti–O photocatalysts prepared as thin films/supported nanocomposites.[39–42] Indeed, the latter are a preferred choice for final end-uses, since they present a lower tendency to sintering/deactivation than powdered PCs and enable to avoid filtration processes required for their recovery.[21,43] Nevertheless, to the best of our knowledge, no reports on the use of supported Fe_2O_3/TiO_2 composite materials for De-NO_x processes are available in the literature.

Herein, we propose the preparation of supported Fe_2O_3/TiO_2 composite materials by an original low-temperature plasma-assisted strategy, based on the initial PE-CVD of Fe_2O_3 followed by RF-sputtering of moderate TiO_2 amounts. Under controlled conditions, PE-CVD yields highly porous Fe_2O_3 systems with tailored nano-organization,[25,44] whereas RF-sputtering, thanks to its infiltration power, enables an efficient in-depth dispersion of Ti-based species into the Fe_2O_3 matrix,[45,46] resulting in an intimate Fe_2O_3/TiO_2 contact. As already demonstrated, this approach is a highly versatile tool for the fabrication of supported nanomaterials with tunable structure and composition, thanks to the unique activation mechanisms characterizing the adopted non-equilibrium plasmas.[45,46] The utility and flexibility of the latter are indeed due to their high chemical reactivity even in the absence of external thermal supplies, enabling material processing at temperatures lower than conventional vapor-phase routes.[47] As a consequence, PE-CVD processes can be considered more cost-effective than the homologous thermal CVD ones, paving the way to a possible industrial scale-up. Similar observations hold even for RF-sputtering processes, used in the present work for the Fe_2O_3 functionalization with TiO_2.[45]

In this work, beyond the structural, compositional and morphological characterization, the photocatalytic NO_x abatement performances of Fe_2O_3/TiO_2 nanocomposites are presented, with particular attention to the release of toxic intermediates into the outer atmosphere.[48] Remarkably, the obtained systems display a high NO_x removal efficiency, superior to that evaluated for Degussa P25 and other modified TiO_2-based materials.[1,3,49]

2 Experimental

2.1 Synthesis

Fe_2O_3 depositions were carried out by means of a two-electrode custom-built PE-CVD apparatus ($\nu = 13.56$ MHz).[50] Depositions were performed on p-type Si(100) substrates (MEMC®, Merano, Italy, 30 mm × 30 mm × 1 mm), subjected to an established cleaning procedure prior to each deposition.[25] Electronic grade argon and oxygen were used as plasma sources. The iron precursor, $Fe(dpm)_3$ (dpm = 2,2,6,6-tetramethyl-3,5-heptanedionate), synthesized as recently reported,[44] was placed in an external glass vaporizer heated at 130 °C with an oil bath, and transported into the reaction chamber by an Ar flow [rate = 60 standard cubic centimeters per minute (sccm)]. Two further auxiliary gas-lines were used to separately introduce Ar and O_2 (flow rates = 15 and 20 sccm, respectively) directly into the reaction chamber. To prevent detrimental condensation phenomena, the delivery gas lines were maintained at 160 °C by means of external heating tapes. After preliminary optimization experiments aimed at ensuring the reproducibility of sample characteristics, the growth parameters were set as follows: inter-electrode distance = 6 cm; deposition time = 60 min; RF-power = 20 W; substrate temperature = 100 °C; total pressure = 1.0 mbar. In the following, the bare iron oxide reference sample is labeled as Fe_2O_3.

Subsequently, functionalization with TiO_2 was performed by RF-sputtering, using the above-described apparatus, and Ar as plasma source. A Ti target (Alfa Aesar®; thickness = 0.3 mm; purity = 99.95%) was fixed on the RF-electrode. The TiO_2 sputtering parameters were optimized basing on preliminary deposition experiments aimed at avoiding a too thick TiO_2 layer, that would have negatively affected the porosity of the underlying Fe_2O_3 matrix. Sputtering processes were carried out under the following conditions: substrate temperature = 60 °C; RF power = 20 W; total pressure = 0.3 mbar; Ar flow rate = 10 sccm; duration = 2 h (sample FeTi2) or 4 h (sample FeTi4). In addition, to obtain a comparison for the nanocomposite functional performances, pure TiO_2 specimens were fabricated by sputtering for 4 h on Si(100) (sample TiO_2). Under the adopted conditions, the thickness of the TiO_2 deposit was estimated to be lower than 5 nm.

For comparison purposes, commercially available TiO_2 P25 was used as a reference photocatalyst (10 mg of powders in a sample holder of 30 mm × 30 mm).

2.2 Characterization

The deposit mass was measured by using a Mettler Toledo XS105DU Microbalance (average weight = 0.55 ± 0.05 mg).

XRD measurements were run at a fixed incidence angle of 1.0° by means of a Bruker D8 Advance instrument equipped with a Göbel mirror, using a CuKα X-ray source ($\lambda = 1.54056$ Å).

FE-SEM micrographs were collected by a Zeiss SUPRA 40VP instrument, using primary beam acceleration voltages of 10 kV.

AFM analyses were carried out by using a Bruker Dimension Icon AFM (Digital Instruments) operated in tapping mode and in air. Images were recorded on different sample areas in order

to check surface homogeneity. Root-mean-square (RMS) roughness values were calculated from the height profile of $2.0 \times 2.0\ \mu m^2$ micrographs.

XPS measurements were performed by using a Perkin-Elmer Φ5600ci spectrometer with a non-monochromatized AlKα source ($h\nu = 1486.6$ eV). Charging effects were corrected by assigning a binding energy (BE) of 284.8 eV to the adventitious C 1s signal. The estimated uncertainty on BE values was ± 0.2 eV. After a Shirley-type background subtraction, raw spectra were fitted by adopting Gaussian–Lorentzian peak shapes.[51] The surface titanium molar fraction was calculated basing on Ti and Fe atomic percentages (at%), according to the following relation:

$$X_{Ti} = \text{Ti at\%}/(\text{Ti at\%} + \text{Fe at\%}) \times 100 \quad (1)$$

In-depth SIMS analyses were carried out by means of a IMS 4f mass spectrometer (Cameca) using a 14.5 keV Cs^+ primary beam (current = 25 nA, stability = 0.3%) and by negative secondary ion detection, using an electron gun for charge compensation. Beam blanking mode and high mass resolution configuration were adopted. The target signals were recorded by rastering over a $175 \times 175\ \mu m^2$ area and detecting secondary ions from a sub-region of $7 \times 7\ \mu m^2$, in order to avoid the occurrence of crater effects.

Infrared (IR) spectra were recorded by means of a Perkin Elmer FTIR System Spectrum BX, operating in transmittance mode at normal incidence.

2.3 Photocatalytic tests

Photocatalytic De-NO_x experiments were performed at room temperature using a protocol similar to the standardized one developed for the characterization of air-purification performances.[52] In particular, taking into account the sample geometric area (9.0 cm^2) and the low average deposit mass (0.55 $\pm$ 0.05 mg), a small-sized reactor (volume = 50 cm^3) and an NO concentration of 100 ppb (obtained by mixing synthetic air and pure NO) were deliberately chosen, in order to achieve an optimal sensitivity. To this aim, it is worthwhile noticing that a similar NO content, representative of NO concentrations found during intense photochemical pollution events in urban environments,[53] was already successfully adopted not only in our previous research works,[29,54] but also in the studies carried out by other investigators.[16,55]

In each experiment, the NO flow was passed over the sample, placed inside the reaction chamber and irradiated from the top through a quartz window. The reactor was placed inside a light sealed irradiation box (Solarbox 3000e RH) equipped with a Xe lamp and illuminated with artificial sunlight. UV and Vis irradiance (25 and 580 W m^{-2}, respectively) were adjusted by a Delta Ohm HD 232.0 photo-radiometer provided with LP 471 UV (λ = 315–400 nm) and LP 471 RAD (λ = 400–1050 nm) irradiance probes. Synthetic air (flow rate = 0.30 L min^{-1}) was passed through a gas-washing bottle, filled with demineralized water in order to maintain a constant relative humidity level [(50 $\pm$ 5)%]. Prior to each test, the air/NO mixture was pre-fluxed over the sample in the dark for 10 min, in order to ensure a proper system stabilization. Under these conditions, no variation in the NO and NO_2 concentration profiles was observed, enabling thus to discard any relevant NO_x adsorption/degradation phenomenon on the sample surface. Subsequently, irradiation for 60 min was performed. Nitrogen oxides concentrations as a function of illumination time were measured using a chemiluminescence analyzer (Environment AC32M). The tests were repeated three times to obtain average concentration values. The calculated standard deviation is ± 0.3 ppb for NO concentration, and ± 1.0 ppb for NO_2 and NO_x concentration.

NO conversion, NO_2 released and NO_x conversion were defined as follows:

$$\text{NO conversion (\%)} = \{([NO]_{in} - [NO]_{out})/[NO]_{in}\} \times 100 \quad (2)$$

$$NO_2 \text{ released (\%)} = ([NO_2]_{out}/[NO]_{in}) \times 100 \quad (3)$$

$$NO_x \text{ conversion (\%)} = \{([NO_x]_{in} - [NO_x]_{out})/[NO_x]_{in}\} \times 100 \quad (4)$$

where $[NO]_{in}$, $[NO_x]_{in}$ and $[NO]_{out}$, $[NO_2]_{out}$, $[NO_x]_{out}$ denote the measured inlet and outlet concentrations, respectively, while $[NO_x] = [NO] + [NO_2]$. The used values were the average of the measured one under steady state period (irradiation time: 40–70 min).

The system selectivity, S, is determined according to eqn (5):[56]

$$S(\%) = \frac{([NO_x]_{in} - [NO_x]_{out})/[NO_x]_{in}}{([NO]_{in} - [NO]_{out})/[NO]_{in}} \times 100 \quad (5)$$

3 Results and discussion

The Fe_2O_3/TiO_2 specimens synthesized in the present work were fabricated using two different Ti sputtering times [2 h (FeTi2), and 4 h (FeTi4)], in order to obtain two different loadings and spatial distribution of TiO_2 into the iron oxide matrix.

The system structure and phase composition were preliminarily investigated by XRD analyses. XRD patterns of Fe_2O_3-containing systems (ESI Fig. S1†) evidenced Bragg reflections of the rhombohedral *hematite* (α-Fe_2O_3) phase.[57] In addition, the higher intensity of the (110) signal with respect to the (104) one may suggest a preferential alignment of the [110] axis perpendicularly to the substrate (*i.e.*, *c*-oriented growth).[58] Irrespective of the adopted sputtering time, no diffraction peaks corresponding to TiO_2 polymorphs or to ternary Fe–Ti–O phases were detected, likely due to the low TiO_2 amount.[22,28,46,59]

For the same reason, no appreciable titania reflections could be detected for the bare TiO_2 specimen. The presence of TiO_2 was however confirmed by compositional analyses (see below).

In order to investigate the surface and in-depth chemical composition, XPS and SIMS analyses were performed, focusing in particular on iron and titanium chemical states and on their mutual distribution throughout the deposit thickness. For all systems, the presence of Fe, Ti and O XPS surface peaks was detected, along with a minor contribution

from adventitious carbon arising from atmospheric exposure (ESI Fig. S2†). In line with XRD results, the spectral features of the Fe 2p signal [BE (Fe $2p_{3/2}$) = 711.2 eV, Fig. 1a] were similar for all specimens and confirmed Fe_2O_3 presence.[25,28,44–46,60] As a matter of fact, surface iron signals could be detected even for the higher titanium loadings (≈11 at% after 4 h of sputtering, sample FeTi4).

Two different components contributed to the O 1s surface signal (Fig. 1b). Beside a major band at 530.0 eV [(I), 67% of the overall O content], related to M–O–M bonds (M = Fe, Ti), a second component (II) at higher BE (531.6 eV) was attributed to hydroxyl/carbonate species arising from exposure to the outer atmosphere.[21,25,46] Irrespective of the sputtering time, Ti $2p_{3/2}$ BE values (458.8 eV, Fig. 1c) were in line with TiO_2 presence and enabled to exclude the formation of Fe–Ti–O ternary phases.[21,28,59,60] The surface titanium molar fraction (Fig. 1d) displayed a linear increase with sputtering time, indicating thus the possibility of exerting a fine control over the system surface properties by tuning the preparative conditions.

Since the mutual distribution of Fe_2O_3 and TiO_2 is a key issue for an optimal nanocomposite engineering, a further insight into the system composition was achieved by in-depth SIMS analyses (Fig. 2). In both nanocomposites, Ti ionic yield underwent a progressive decrease within the first seconds of erosion, and subsequently reached an almost constant value. These phenomena, particularly evident for the specimen characterized by the highest TiO_2 loading (FeTi4), indicated a titania accumulation in the near-surface system layers. Nevertheless, the presence of Ti signal up to the interface with the Si substrate suggested that TiO_2 was present even in the inner *hematite* regions. This finding, attributed to the synergistic coupling of the Fe_2O_3 porosity (see below) and the sputtering infiltration power, resulted in an intimate TiO_2/Fe_2O_3 coupling, a key issue

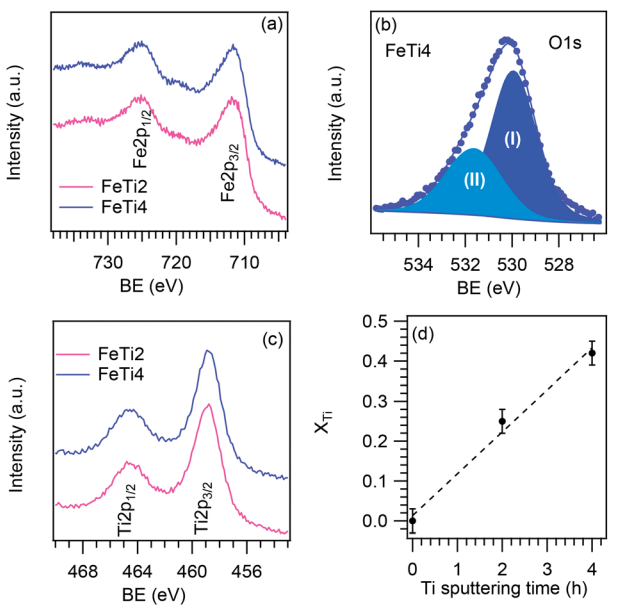

Fig. 1 Surface XPS photoelectron peaks for: (a) Fe 2p, (b) O 1s and (c) Ti 2p. (d) Surface titanium molar fraction as a function of the used sputtering time.

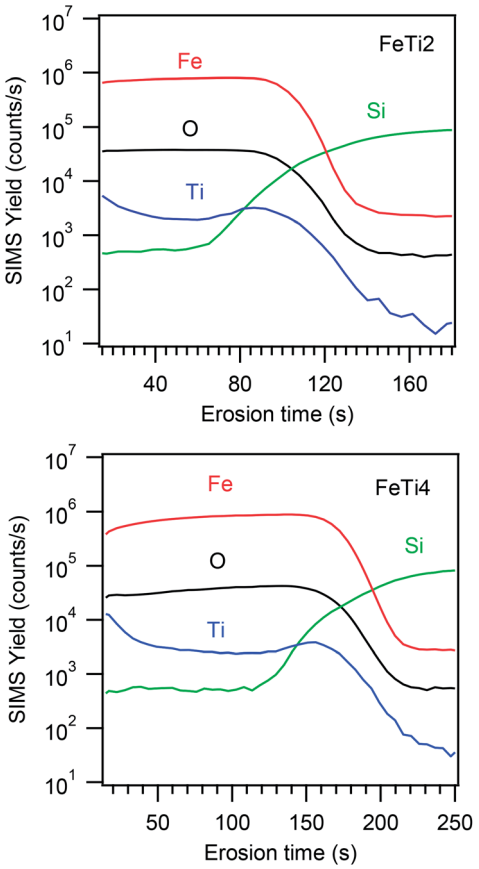

Fig. 2 SIMS in-depth profiles for Fe_2O_3/TiO_2 specimens.

to exploit their mutual interplay for the target functional applications.

The system morphological organization was investigated by FE-SEM analyses. As can be appreciated in ESI Fig. S3,† bare iron oxide presented interconnected leaf-like nanostructures (mean lateral size = 20 nm; mean deposit thickness = 150 nm), characterized by a cross-section columnar habit. The arrangement of such structures resulted in the obtainment of highly porous systems, amenable candidates for solar-driven applications, as well as for the subsequent functionalization with phases, like TiO_2.[21,45,46] In fact, the reduced lateral size of Fe_2O_3 nanostructures is a key tool to improve charge carrier transport and light harvesting properties, since they have a long axis enabling an efficient sunlight absorption and a short radial distance for the diffusion of photogenerated carriers to the material surface.[46]

Upon TiO_2 introduction (Fig. 3), Fe_2O_3 morphology did not undergo dramatic modifications, thanks to the use of relatively mild processing conditions.[45,46] A detailed comparison of FE-SEM micrographs in Fig. 3 and S3† revealed indeed that the systems morphology become slightly more rounded upon TiO_2 deposition. This effect directly depended on Ti sputtering time (and loading), since it was more evident for the FeTi4 specimen. In any case, the TiO_2 overlayer thickness could not be clearly measured. The present results, in line with those recently reported for Fe_2O_3/Co_3O_4 composites fabricated by a similar

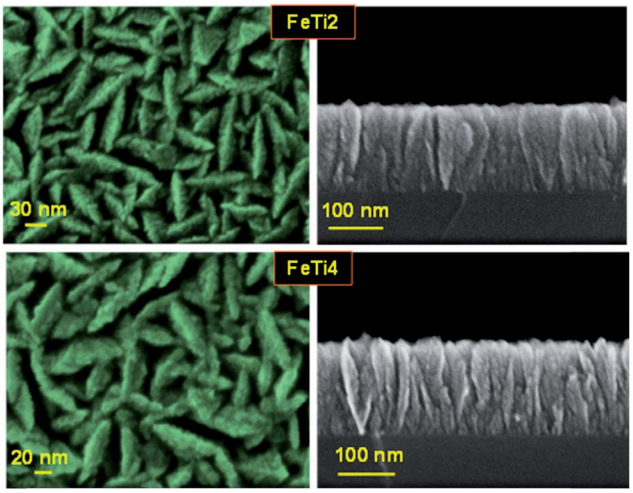

Fig. 3 Plane view (left) and cross sectional (right) FE-SEM micrographs for FeTi2 and FeTi4 samples.

route,[46] were further supported by AFM analyses, that did not reveal appreciable differences between the bare Fe_2O_3 and FeTi4 sample with the highest Ti loading (compare ESI Fig. S4†). Taking into account also the above discussed XRD and XPS results, these findings suggest either a high dispersion of Ti-containing species, or the formation of a very thin/porous titania overlayer.[28] As already observed, the intimate contact between the two oxides, that was achieved without any detrimental alteration of the pristine Fe_2O_3 porosity, is a key feature to synergistically exploit Fe_2O_3/TiO_2 heterojunction and cooperative effects in photocatalytic applications. To this regard, the present materials were tested in NO_x photocatalytic abatement. The complete oxidation of NO to nitrate or nitric acid (NO_3^-/HNO_3) is a complex process, that involves several intermediate species.[48,61,62] Basically, the mechanism entails several one-electron transfer steps, *via* nitrous acid (HNO_2) and nitrogen dioxide (NO_2) as intermediate species. The *in situ* generated reactive oxygen species (mainly hydroxyl radicals but also superoxides; see also below and ESI Fig. S7†) assist as strong oxidants the process, whose steps can be sketched as follows:[56,63,64]

$$NO \xrightarrow{OH^\cdot} HNO_2 \xrightarrow{OH^\cdot} NO_2 \xrightarrow{OH^\cdot} HNO_3 \quad (6)$$

Fig. 4 displays the NO, NO_2 and total nitrogen oxide (NO_x) concentration profiles recorded for different specimens as a function of irradiation time. It is worth recalling that photocatalytic experiments were carried out by flowing 100 ppb of NO into a flow-through reactor. As can be observed from Fig. 4a, during the first 10 min in the dark the concentration of NO remained constant, highlighting the crucial role of sunlight exposure to activate the process. Subsequently, under irradiation from 10 to 70 min, a significant NO signal decrease was observed, evidencing the occurrence of a light-induced chemical reaction on Fe_2O_3/TiO_2 surfaces.[3,16] The constant NO values

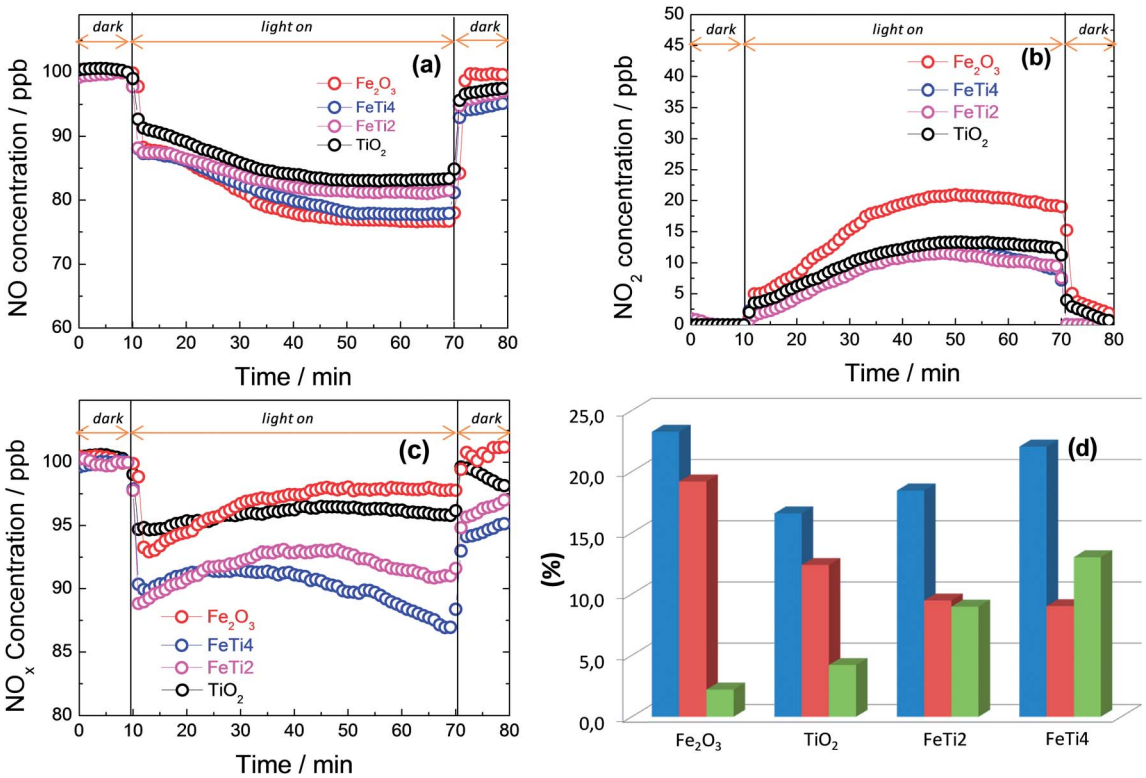

Fig. 4 (a–c) Nitrogen oxides concentration profiles obtained during the photo-degradation of gaseous NO under sunlight irradiation on Fe_2O_3/TiO_2 composite systems. The curves pertaining to bare TiO_2 and bare Fe_2O_3 are also shown for comparison. (d) NO conversion (%, blue), NO_2 released (%, red) and NO_x conversion (%, green) for Fe_2O_3, FeTi2, FeTi4 and TiO_2 samples.

achieved after 40 min indicated that a steady state condition of maximum activity was reached. Finally, upon illumination shutdown, the NO concentration returned almost to its initial value.

The difference in values measured between dark and light conditions is related to the amount of removed NO. As can be observed from Fig. 4a, NO conversion values were higher than 15% for all samples, and reached a maximum value close to 25% for bare Fe_2O_3, corresponding to an almost doubled efficiency if compared to that previously reported for powdered *hematite*.[54] However, an effective air quality improvement does not rely on the sole NO removal, but also on suppression of undesired intermediates (in particular NO_2).[56] Hence, the photocatalyst performances should be evaluated also in terms of NO_2 formation and total NO_x removal. To this aim, Fig. 4b evidences that non-negligible NO_2 amounts are released during the irradiation of bare Fe_2O_3 samples, suggesting that, in this case, NO is mainly oxidized to NO_2. As observed in Fig. 4c, the NO_x removal results very poor (3%) for bare Fe_2O_3. This phenomenon was attributed to the inherent *hematite* drawbacks, and, in particular, to its short excited-state lifetime, which, in turn, promotes a fast recombination[26] and prevent the formation of $OH^{\bullet}$ in sufficient amount to complete photo-oxidation processes (6).[54] In a different way, the use of composite Fe_2O_3/TiO_2 systems resulted in an appreciable decrease of the released NO_2 amount (Fig. 4b). Furthermore, as displayed in Fig. 4c, the overall NO_x removal increased, yielding nearly twofold (FeTi2) and threefold (FeTi4) performances compared to bare Fe_2O_3 (see also Fig. 4d). In addition, the De-NO_x action exhibited by composite samples was higher than that tested for the bare TiO_2 sample prepared for comparison purposes (Fig. 4d). Another important benefit of the Fe_2O_3/TiO_2 interaction is evidenced by their PC activity under the sole Vis light illumination. As can be noticed from Fig. S5 in the ESI,† that compares the PC performances of representative samples under Vis irradiation, the reactivity order was $TiO_2 \ll Fe_2O_3 <$ FeTi4. In particular, the activity of bare TiO_2 was almost negligible, due to the large titania band-gap preventing visible light absorption. In a different way, NO abatement was clearly evident on bare Fe_2O_3, as a consequence of its lower band-gap. Remarkably, upon going from bare Fe_2O_3 to FeTi4, a further activity improvement was detected. This effect can not be due to TiO_2 light absorption properties but, rather, to the formation of Fe_2O_3/TiO_2 junctions, enhancing hole lifetime and promoting charge carrier separation. Furthermore, thanks to titania favourable properties, the latter effect can also boost the formation of $OH^{\bullet}$ species in sufficient amount to complete NO photo-oxidation.

The possibility of photocatalyst reuse has been preliminarily investigated for FeTi4, the most active specimen. The obtained results (ESI Fig. S6†) displayed a modest activity loss ($\approx$14%) in the first few cycles of reutilization, and a subsequent activity stabilization from the fifth cycle. In order to properly interpret this result, it is worth noticing that the sample was rinsed with water between consecutive cycles in order to eliminate nitrite/nitrate species. Even though the identification of an appropriate cleaning procedure for the target specimens is not a straightforward task and will require additional efforts, the data collected so far suggest that no significant photocatalyst degradation took place under the adopted experimental conditions. Taken together, these results clearly highlight the beneficial synergy between Fe_2O_3 and TiO_2, resulting in improved photocatalytic performances. As reported also for other composite systems, the main advantages of Fe_2O_3 and TiO_2 coupling can be traced back not only to the improved solar light harvesting in the Vis range with respect to bare TiO_2, but also to the minimized electron–hole recombination and faster photogenerated charge transfer at the Fe_2O_3/TiO_2 interface (ESI Fig. S7†).[30,31,65–67] In this way, the holes accumulated in the valence band assist the formation of $OH^{\bullet}$ radicals that can further contribute to the progressive NO oxidation (6), whereas electron accumulated in the conduction band can favor the generation of O_2^{-} species, directly involved in the process (see above).[21]

Fig. 5 shows a comparison of the photocatalytic NO_x abatement selectivity (S) for bare Fe_2O_3 and Fe_2O_3/TiO_2 composites. This parameter expresses the ratio of degraded NO that is ultimately converted into harmless nitrate, rather than into toxic nitrogen dioxide. As can be appreciated, the selectivity underwent a remarkable enhancement upon increasing TiO_2 loading and, in particular, the sample with the highest TiO_2 content (FeTi4) displayed a value as high as 63%. Interestingly, this value exceeded that reported for the standard TiO_2 P25 (S = 25%), used as benchmark in similar processes, and of other modified TiO_2-based materials investigated in previous works (45% < S < 53%),[1,3,49] validating thus the significance of the present results in eventual practical applications. The highest S

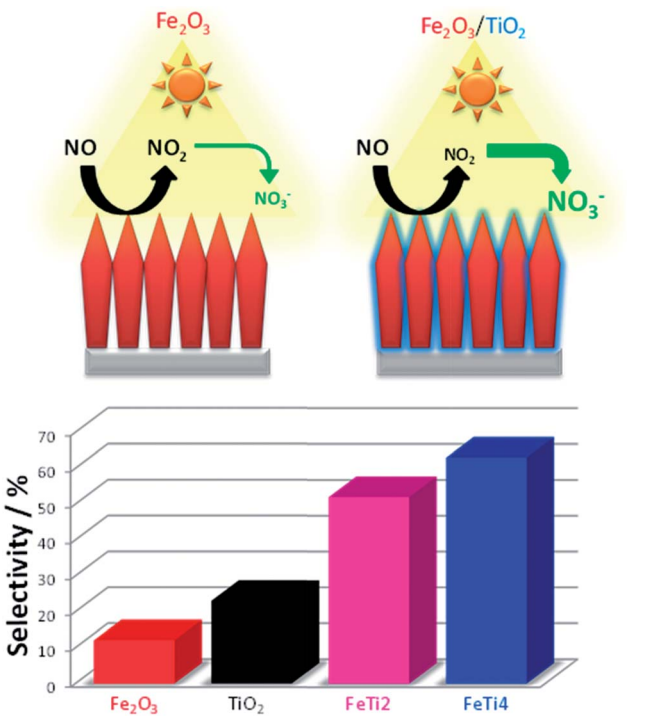

Fig. 5 NO abatement selectivity values for the target specimens investigated in the present work.

values obtained herein indicate the occurrence of good performances for the NO → NO_2 → NO_3^- oxidation process (6).

In order to further support this conclusion, and validate the selectivity values measured from the NO_x concentration profiles, IR spectra of the most efficient photocatalyst (FeTi4) and bare Fe_2O_3 (ESI Fig. S8†) were collected before and after irradiation, to investigate the presence of possible adsorbed products.

Considering that during PC experiments only a few ppbs of nitrite/nitrate species were formed, a detailed observation in the IR region characteristic for nitrite/nitrate vibration modes (1800–1200 cm^{-1}) is requested to evidence their possible presence. In the case of bare Fe_2O_3 (ESI Fig. S8a†), a low intensity band at 1640 cm^{-1} was observed, corresponding to the absorption of water molecules from the reaction environment onto the surface, whereas no N–O bands were detected. This finding reveals that *hematite* capacity to remove NO_x molecules is negligible, in line with the above results. In a different way, it is worth noting that for the FeTi4 specimen, the most performing one (ESI Fig. S8b†), bands related to NO_2^-/NO_3^- species could be observed in the spectra.

4 Conclusions

Supported Fe_2O_3 nanosystems have been functionalized with tailored TiO_2 amounts by means of a versatile, low temperature plasma-assisted strategy. The adopted synthetic protocol, adopted for the first time in the present investigation, enabled to prevent solid state reactions between Fe_2O_3 and TiO_2 and to fabricate pure and large-area nanocomposites. The target systems were characterized by a tailored morphology and an intimate Fe_2O_3/TiO_2 contact, of strategic importance in view of solar-driven NO oxidation. In particular, an improved De-NO_x efficiency with respect to bare Fe_2O_3 was obtained, highlighting the occurrence of a photocatalytic synergy between the two oxides. In fact, the efficient NO → NO_2^-/NO_3^- conversion could be driven only by Fe_2O_3/TiO_2 nanomaterials, but not by the single components. In contrast to the negligible NO_x amount removed by Fe_2O_3 sample, a selectivity as high as 63% was achieved by Fe_2O_3/TiO_2 nanocomposites. Such values, among the best ever reported in the literature for similar systems, demonstrate the importance of nanocomposite morphological/compositional control in the obtainment of advanced functional performances.

On the basis of the above results, future perspectives for the developments of the present research will concern the detailed analysis of band gap values, VB and CB positions, as well as a deeper understanding of the photocatalytic mechanism by photoluminescence and photoelectrochemical measurements. In addition, further efforts will be devoted to a careful modulation of Fe_2O_3 morphology, to fabricate nanosystems endowed with a higher active area, as well as to the investigation of higher TiO_2 loadings and of their effects on the ultimate functional behavior. In this way, the high potential of the proposed approach for De-NO_x process triggered not only by solar light, but even by the sole Vis illumination, will be fully exploited in real-world end-uses for environmental remediation.

Acknowledgements

The research leading to these results has received funding from the FP7 project "SOLAROGENIX" (NMP4-SL-2012-310333). Padova University ex-60% 2012–2015, SOLLEONE (CPDR132937/13) and ACTION projects, are also gratefully acknowledged. In addition, this work was partially funded by Junta de Andalucía (Group FQM-175) and Córdoba University (XX PP. Modalidad 4.1).

Notes and references

1 J. Ângelo, L. Andrade and A. Mendes, *Appl. Catal., A*, 2014, **484**, 17–25.
2 J. Colls, *Air Pollution*, Spon Press, London, New York, 2002.
3 J. Ma, H. Wu, Y. Liu and H. He, *J. Phys. Chem. C*, 2014, **118**, 7434–7441.
4 H. A. Habib, R. Basner, R. Brandenburg, U. Armbruster and A. Martin, *ACS Catal.*, 2014, **4**, 2479–2491.
5 A. Folli, S. B. Campbell, J. A. Anderson and D. E. Macphee, *J. Photochem. Photobiol., A*, 2011, **220**, 85–93.
6 M. W. Frampton and I. A. Greaves, *Am. J. Respir. Crit. Care Med.*, 2009, **179**, 1077–1078.
7 M. L. Williams and D. C. Carslaw, *Atmos. Environ.*, 2011, **45**, 3911–3912.
8 M. C. Newman and W. H. Clement, *Ecotoxicology: A Comprehensive Treatment*, CRC Press, Boca Raton, Florida, 2008.
9 B. Chen, C. Hong and H. Kan, *Toxicol.*, 2004, **198**, 291–300.
10 S. A. Cormier, S. Lomnicki, W. Backes and B. Dellinger, *Environ. Health Perspect.*, 2006, **114**, 810–817.
11 A. Yamamoto, Y. Mizuno, K. Teramura, S. Hosokawa and T. Tanaka, *ACS Catal.*, 2015, **5**, 2939–2943.
12 C. S. Poon and E. Cheung, *Construct. Build. Mater.*, 2007, **21**, 1746–1753.
13 R. Sugrañez, J. I. Álvarez, M. Cruz-Yusta, I. Mármol, J. Morales, J. Vila and L. Sánchez, *Build. Environ.*, 2013, **69**, 55–63.
14 S. Karapati, T. Giannakopoulou, N. Todorova, N. Boukos, D. Dimotikali and C. Trapalis, *Appl. Catal., B*, 2015, **176–177**, 578–585.
15 H. Chen, C. E. Nanayakkara and V. H. Grassian, *Chem. Rev.*, 2012, **112**, 5919–5948.
16 M. E. Monge, B. D'Anna and C. George, *Phys. Chem. Chem. Phys.*, 2010, **12**, 8991–8998.
17 M. Pelaez, N. T. Nolan, S. C. Pillai, M. K. Seery, P. Falaras, A. G. Kontos, P. S. M. Dunlop, J. W. J. Hamilton, J. A. Byrne, K. O'Shea, M. H. Entezari and D. D. Dionysiou, *Appl. Catal., B*, 2012, **125**, 331–349.
18 A. Petala, E. Ioannidou, A. Georgaka, K. Bourikas and D. I. Kondarides, *Appl. Catal., B*, 2015, **178**, 201–209.
19 L. He, L. Jing, Y. Luan, L. Wang and H. Fu, *ACS Catal.*, 2014, **4**, 990–998.
20 A. Trapalis, N. Todorova, T. Giannakopoulou, N. Boukos, T. Speliotis, D. Dimotikali and J. Yu, *Appl. Catal., B*, 2016, **180**, 637–647.

21 D. Barreca, G. Carraro, M. E. A. Warwick, K. Kaunisto, A. Gasparotto, V. Gombac, C. Sada, S. Turner, G. Van Tendeloo, C. Maccato and P. Fornasiero, *CrystEngComm*, 2015, **17**, 6219–6226.

22 S. Zhu, F. Yao, C. Yin, Y. Li, W. Peng, J. Ma and D. Zhang, *Microporous Mesoporous Mater.*, 2014, **190**, 10–16.

23 D. Barreca, G. Carraro, A. Gasparotto, C. Maccato, F. Rossi, G. Salviati, M. Tallarida, C. Das, F. Fresno, D. Korte, U. Lavrenčič Štangar, M. Franko and D. Schmeisser, *ACS Appl. Mater. Interfaces*, 2013, **5**, 7130–7138.

24 H. Tang, D. Zhang, G. Tang, X. Ji, W. Li, C. Li and X. Yang, *Ceram. Int.*, 2013, **39**, 8633–8640.

25 G. Carraro, A. Gasparotto, C. Maccato, E. Bontempi and D. Barreca, *Chem. Vap. Deposition*, 2015, **21**, 294–299.

26 D. A. Wheeler, G. Wang, Y. Ling, Y. Li and J. Z. Zhang, *Energy Environ. Sci.*, 2012, **5**, 6682–6702.

27 M. Mishra and D.-M. Chun, *Appl. Catal., A*, 2015, **498**, 126–141.

28 M. G. Ahmed, I. E. Kretschmer, T. A. Kandiel, A. Y. Ahmed, F. A. Rashwan and D. W. Bahnemann, *ACS Appl. Mater. Interfaces*, 2015, **7**, 24053–24062.

29 G. Carraro, R. Sugrañez, C. Maccato, A. Gasparotto, D. Barreca, C. Sada, M. Cruz-Yusta and L. Sánchez, *Thin Solid Films*, 2014, **564**, 121–127.

30 X. Yang, J. Qin, Y. Jiang, K. Chen, X. Yan, D. Zhang, R. Li and H. Tang, *Appl. Catal., B*, 2015, **166–167**, 231–240.

31 X. Yang, J. Qin, Y. Jiang, R. Li, Y. Li and H. Tang, *RSC Adv.*, 2014, **4**, 18627–18636.

32 X. Yang, J. Qin, Y. Li, R. Zhang and H. Tang, *J. Hazard. Mater.*, 2013, **261**, 342–350.

33 W.-K. Jo and N. C. S. Selvam, *Dalton Trans.*, 2015, **44**, 16024–16035.

34 S. J. A. Moniz, S. A. Shevlin, X. An, Z.-X. Guo and J. Tang, *Chem.–Eur. J.*, 2014, **20**, 15571–15579.

35 X. Zhang, Y. Xie, H. Chen, J. Guo, A. Meng and C. Li, *Appl. Surf. Sci.*, 2014, **317**, 43–48.

36 Y. Xia and L. Yin, *Phys. Chem. Chem. Phys.*, 2013, **15**, 18627–18634.

37 P. Zhang, S. Yin and T. Sato, *Appl. Catal., B*, 2011, **103**, 462–469.

38 J. Y. Kim, C. S. Kim, H. K. Chang and T. O. Kim, *Adv. Powder Technol.*, 2011, **22**, 443–448.

39 M. A. Mahadik, S. S. Shinde, V. S. Mohite, S. S. Kumbhar, A. V. Moholkar, K. Y. Rajpure, V. Ganesan, J. Nayak, S. R. Barman and C. H. Bhosale, *J. Photochem. Photobiol., B*, 2014, **133**, 90–98.

40 P. Ctibor, Z. Pala, V. Stengl and R. Musalek, *Ceram. Int.*, 2014, **40**, 2365–2372.

41 X. Zhang and L. Lei, *Appl. Surf. Sci.*, 2008, **254**, 2406–2412.

42 S. Sathasivam, D. S. Bhachu, Y. Lu, S. M. Bawaked, A. Y. Obaid, S. Al-Thabaiti, S. N. Basahel, C. J. Carmalt and I. P. Parkin, *Chem. Vap. Deposition*, 2015, **21**, 21–25.

43 D. Barreca, G. Carraro, V. Gombac, A. Gasparotto, C. Maccato, P. Fornasiero and E. Tondello, *Adv. Funct. Mater.*, 2011, **21**, 2611–2623.

44 G. Carraro, C. Maccato, A. Gasparotto, D. Barreca, M. Walter, L. Mayrhofer, M. Moseler, A. Venzo, R. Seraglia and C. Marega, *Phys. Chem. Chem. Phys.*, 2015, **17**, 11174–11181.

45 G. Carraro, A. Gasparotto, C. Maccato, E. Bontempi, F. Bilo, D. Peeters, C. Sada and D. Barreca, *CrystEngComm*, 2014, **16**, 8710–8716.

46 G. Carraro, C. Maccato, A. Gasparotto, K. Kaunisto, C. Sada and D. Barreca, *Plasma Processes Polym.*, 2016, **13**, 191–200.

47 A. Gasparotto, D. Barreca, D. Bekermann, A. Devi, R. A. Fischer, C. Maccato and E. Tondello, *J. Nanosci. Nanotechnol.*, 2011, **11**, 8206–8213.

48 J. Balbuena, M. Cruz-Yusta and L. Sánchez, *J. Nanosci. Nanotechnol.*, 2015, **15**, 6373–6385.

49 M. Polat, A. M. Soylu, D. A. Erdogan, H. Erguven, E. I. Vovk and E. Ozensoy, *Catal. Today*, 2015, **241**, 25–32.

50 D. Barreca, A. Gasparotto, E. Tondello, C. Sada, S. Polizzi and A. Benedetti, *Chem. Vap. Deposition*, 2003, **9**, 199–206.

51 D. Briggs and M. P. Seah, *Practical Surface Analysis: Auger and X-ray Photoelectron Spectroscopy*, John Wiley & Sons, New York, 2nd edn, 1990.

52 ISO 22197-1, *Fine ceramics (advanced ceramics, advanced technical ceramics); test method for air purification performance of semiconducting photocatalytic materials, Part 1: removal of nitric oxide*, 2007.

53 S. K. Pandey, K.-H. Kim, S.-Y. Chung, S. J. Cho, M. Y. Kim and Z.-H. Shon, *Atmos. Environ.*, 2008, **42**, 607–622.

54 R. Sugrañez, J. Balbuena, M. Cruz-Yusta, F. Martín, J. Morales and L. Sánchez, *Appl. Catal., B*, 2015, **165**, 529–536.

55 M. Signoretto, E. Ghedini, V. Trevisan, C. L. Bianchi, M. Ongaro and G. Cruciani, *Appl. Catal., B*, 2010, **95**, 130–136.

56 J. Z. Bloh, A. Folli and D. E. Macphee, *RSC Adv.*, 2014, **4**, 45726–45734.

57 Pattern No. 33-0664, JCPDS, 2000.

58 M. E. A. Warwick, K. Kaunisto, D. Barreca, G. Carraro, A. Gasparotto, C. Maccato, E. Bontempi, C. Sada, T.-P. Ruoko, S. Turner and G. Van Tendeloo, *ACS Appl. Mater. Interfaces*, 2015, **7**, 8667–8676.

59 D. Barreca, G. Carraro, A. Gasparotto, C. Maccato, O. I. Lebedev, A. Parfenova, S. Turner, E. Tondello and G. Van Tendeloo, *Langmuir*, 2011, **27**, 6409–6417.

60 J. F. Moulder, W. F. Stickle, P. E. Sobol and K. D. Bomben, *Handbook of X-ray Photoelectron Spectroscopy*, Perkin Elmer Corporation, Eden Prairie, MN, USA, 1992.

61 J. Lasek, Y.-H. Yu and J. C. S. Wu, *J. Photochem. Photobiol., C*, 2013, **14**, 29–52.

62 S. Laufs, G. Burgeth, W. Duttlinger, R. Kurtenbach, M. Maban, C. Thomas, P. Wiesen and J. Kleffmann, *Atmos. Environ.*, 2010, **44**, 2341–2349.

63 S. Devahasdin, C. Fan Jr, K. Li and D. H. Chen, *J. Photochem. Photobiol., A*, 2003, **156**, 161–170.

64 M. Kaneko and I. Okura, *Photocatalysis: Science and Technology*, Springer, Berlin, Heidelberg, 2002.

65 H. Li, S. Yin, Y. Wang and T. Sato, *Appl. Catal., B*, 2013, **132–133**, 487–492.

66 H. Liu, H. K. Shon, X. Sun, S. Vigneswaran and H. Nan, *Appl. Surf. Sci.*, 2011, **257**, 5813–5819.

67 R. S. Wade and C. E. Castro, *Chem. Res. Toxicol.*, 1996, **9**, 1382–1390.